FEASIBILITY ASSESSMENT: A CYCLOIDAL ROTOR TO REPLACE CONVENTIONAL HELICOPTER TECHNOLOGY

Louis Gagnon*, Marco Morandini, Giuseppe Quaranta, Vincenzo Muscarello,
Pierangelo Masarati, Giampiero Bindolino
Dipartimento di Scienze e Tecnologie Aerospaziali, Politecnico di Milano, via La Masa 34, 20156, Milano, Italy
louis.gagnon,marco.morandini,giuseppe.quaranta@polimi.it,vincenzo.muscarello
pierangelo.masarati,giampiero.bindolino@polimi.it

Carlos Xisto, José C. Páscoa
Dep. de Eng. Electromecânica, Universidade da Beira Interior, Rua Mq.s D'Ávila e Bolama, 6201-001, Covilhã, Portugal
xisto@ubi.pt, pascoa@ubi.pt

Abstract

A mathematical model is presented for the solution of the aerodynamic performances of a cycloidal rotor. It is solved algebraically for the cases where the forces and incoming wind velocity share the same direction. The model is validated against experimental data coming from three different sources. It is then used to evaluate the viability of using a cycloidal rotor as a replacement for the traditional tail rotor of a helicopter. By doing so, power is saved by the helicopter having non-null advance ratios. The savings reach 50% at an advance ratio of 0.33. It was found that imposing a constant cycloidal rotor angular velocity does not reduce the efficiency and that high pitch angles are the most efficient. The experimental data indicates that three dimensional effects have an influence on the cycloidal rotor performance. A three dimensional Euler fluid dynamic analysis confirms the experimental findings.

1. INTRODUCTION

Cycloidal rotors are a viable means to produce aerodynamic forces whose direction can be rapidly varied in a plane normal to the axis of rotation. The working principle is illustrated on Fig. 1 and a graphical representation of is shown on Fig. 2.

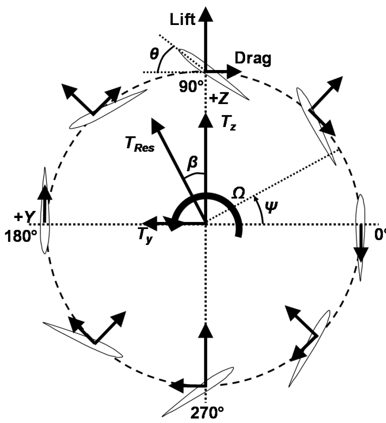

Figure 1: Cycloidal rotor working principle.

In a cycloidal rotor, a drum carries a set of wings, or blades, and their axes are aligned with the rotation axis of the drum. Each blade can pitch about a feathering axis which is also aligned with the rotation axis of the drum.

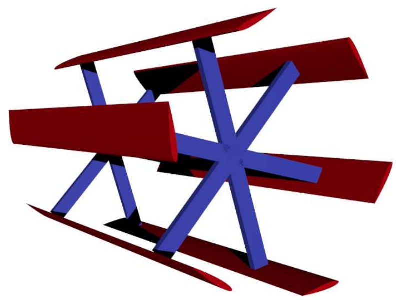

Figure 2: A 6-blade cycloidal rotor viewed from the side.

By pitching the blades with a period equal to that of the drum, a net aerodynamic force normal to the axis of rotation is generated. The direction of the force is controlled by changing the phase of the periodic pitch. Thus, thrust that can be vectored in a plane without moving large mechanical parts. Cycloidal rotors have been studied for their application in vertical axis wind and water turbines.[1–3] Recent studies also investigated their application in unmanned micro aerial vehicles.[4–6] This paper, however, focuses on a manned aircraft application of such rotors.

In this work, a hover-capable vehicle is proposed. It makes use of a conventional helicopter rotor for lift both in hover and forward flight, and uses one or more cycloidal rotors for anti-torque, additional propulsion, and some control. In the explored design configuration, power demanding tasks like lift in hover and in forward flight are delegated to an efficient device, the rotor. The cycloidal rotor replaces existing anti-torque, propulsion and control devices. For such a vehicle, three design solutions were considered and are shown in Fig. 3.

In the first case, Figure 3(a), a cycloidal rotor is mounted on the tail of a conventional helicopter design with the rotor axis along the yaw axis of the vehicle. The cycloidal rotor can provide thrust in a plane normal to the yaw axis. As such, it can act as an anti-torque device and provide propulsion. To obtain a similar effect using a tail rotor, one would need to tilt the entire rotor. The cycloidal rotor only needs to change the pitch of the blades.

In the second case, Figure 3(b), a cycloidal rotor is mounted on the tail of a conventional helicopter design with the rotor axis along the longitudinal axis of the vehicle. The cycloidal rotor can provide thrust in a plane normal to the longitudinal axis. As such, it can act as anti-torque device as well as provide an adaptive capability to stabilize and control the aircraft about the pitch axis. In this case, in forward flight the cycloidal rotor may theoretically experience a significant component of airspeed along the blade axis. This configuration is similar to a patent owned by Eurocopter.

In the third case, Figure 3(c), two cycloidal rotors are mounted on both sides of the airframe with the axis of the rotors along the pitch axis of the vehicle. The rotors provide anti-torque and yaw control by antisymmetric thrust along the fore/aft direction, as well as thrust. They can also contribute to lift, through the vertical component of thrust, and to control about the roll axis. This last configuration is similar to the Eurocopter X^3 and other aircraft known as gyrodynes. They have the additional advantage of vectoring the thrust. Previous work[7,8] shown that this latest configuration is by far the most promising configuration. A concept illustration is shown on Fig. 4.

Figure 4: Cycloidal rotor arrangement which was studied in depth.

To allow the study of the rotor, various aerodynamic and aeroelastic models were developed. Overall, the aerodynamic models were four, being an algebraic, a multibody, a twodimensional CFD, and a threedimensional CFD model. These models were presented in previous articles.[7,8] The results presented here are obtained from a further development of the algebraic model which is explained in detail in the following section.

Finally, this research project is undertaken as part of an European effort for the optimization of cycloidal rotors with the objective of using them in passenger carrying missions. Thus, four universities and two companies from across Europe are part of the Cyloidal Rotor Optimized for Propulsion (CROP) consortium[1].

2. ANALYTICAL AERODYNAMIC MODEL

2.1 Definitions

The algebraic mathematical model allows one to obtain the pitching schedule necessary for a specific cycloidal rotor to produce the wanted thrust and direction. It can be used in the opposite mode, where the pitching schedule is known and the resulting thrust and direction are to be found. The model also allows the computation of the power required by the rotor. It assumes that the lift of a blade is in agreement with a constant slope lift coefficient $a = C_{L/\alpha}$ and a constant drag coefficient C_{D_0}. As a result, it does not consider the effect of blade and wake interaction. A solution is presented for different flight regimes. The schematic of the model is shown in Fig. 5 which represents the side view of the cycloidal rotor, and is in the plane of the supporting arms previously shown in Fig. 2. Three different reference systems are used and are explained in Table 1.

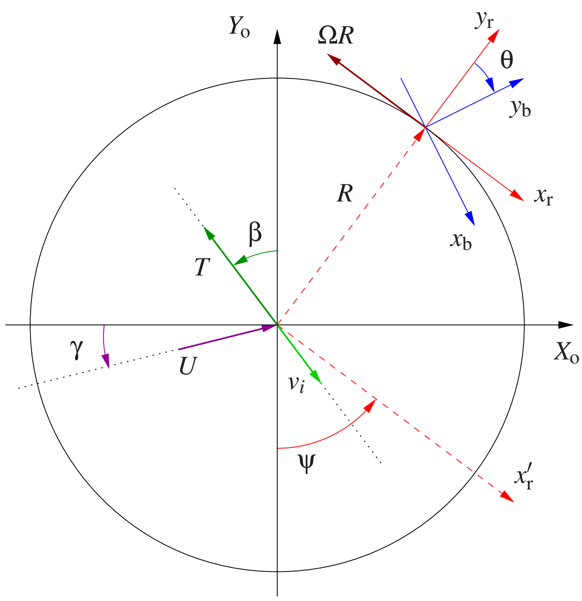

Figure 5: Definition of reference systems.

The thrust T produced is shown on Fig. 5 and acts on the rotor. Its direction is defined as having an angle β with respect to the Y_o axis.

[1]http://crop-project.eu

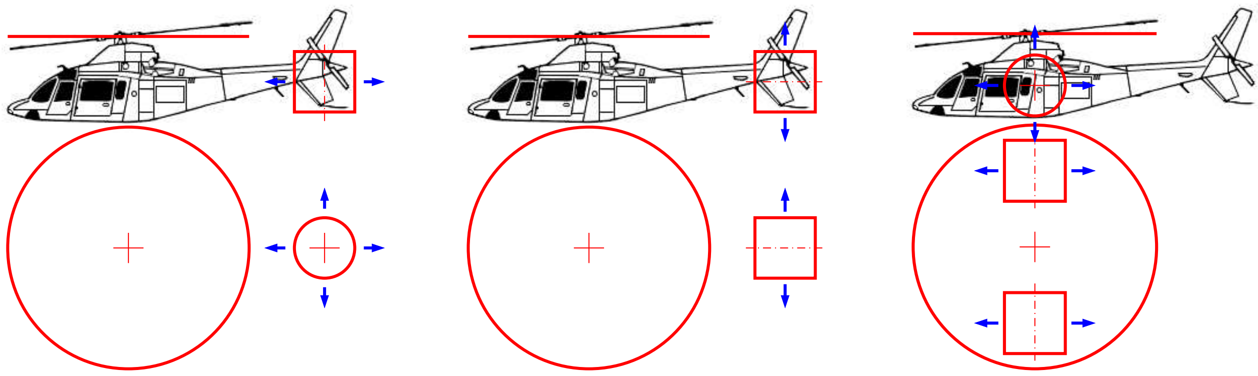

(a) Tail vertical arrangement. (b) Tail longitudinal arrangement. (c) Lateral arrangement.

Figure 3: Cycloidal rotor arrangements considered.

Table 1: Description of the coordinate systems.

System name	Subscript	Description
Basic reference	o	Y_o points in the direction opposite to gravity. X_o is positive towards the right.
Rotating reference	r	y_r is directed radially outward the circular rotor path. x_r is tangent to the circular path and points backwards.
Body reference	b	rotating reference rotated by the pitch angle θ which is positive in the clockwise direction.

Thus,

$$(1)\quad \mathbf{T}_\text{o} = \left\{ \begin{array}{c} -\sin\beta \\ \cos\beta \end{array} \right\} T.$$

An inflow velocity v_i results from the thrust and moves in a direction exactly opposite to the thrust. Thus,

$$(2)\quad \mathbf{v}_{i_\text{o}} = \left\{ \begin{array}{c} \sin\beta \\ -\cos\beta \end{array} \right\} v_i$$

The free airstream velocity U has an angle γ with respect to the horizontal X_o axis. Thus,

$$(3)\quad \mathbf{U}_\text{o} = \left\{ \begin{array}{c} \cos\gamma \\ \sin\gamma \end{array} \right\} U$$

Now that the variables U, v_i, β, T, and γ are defined, the definition of a few typical flight regimes is given in Table 2.

The other typical variables are defined as follows. First, the thrust coefficient is,

$$(4)\quad C_T = \frac{T}{\rho(\Omega R)^2 A},$$

where A is the area of the hollow cylinder described by the path of the cyclorotor blades,

$$(5)\quad A = 2\pi R b,$$

with b being the span of the rotor.

Solidity σ is the ratio of the total area covered by the blades to the ring area A

$$(6)\quad \sigma = \frac{cbN}{2\pi R b} = \frac{cN}{2\pi R},$$

with blade chord c and number of blades N.

Using the simplest momentum theory and referring to Fig. 5 we have a mass flow $\dot{m}$ through the cycloidal rotor given by

$$(7)\quad \begin{aligned} \dot{m} &= \rho A_\text{eff}\sqrt{(v_i\sin(\beta)+U\cos(\gamma))^2+(U\sin(\gamma)-v_i\cos(\beta))^2} \\ &= \rho A_\text{eff}\sqrt{U^2+v_i^2+2Uv_i\sin(\beta-\gamma)} \end{aligned}$$

where $A_\text{eff} = 2Rb$ is the area of an ideal stream tube that runs across the drum, perpendicular to the drum axis.

And since the thrust T is equal to the rate of change of the momentum, we obtain that,

$$(8)\quad \begin{aligned} T &= \dot{m}w \\ &= 2\dot{m}v_i \end{aligned}$$

where w is the velocity at the end of the streamtube defined by the momentum theory applied to the cycloidal rotor in a fashion inspired by Johnson.[9]

The induced velocity can be expressed as,

$$(9)\quad \begin{aligned} v_i &= \frac{T/(2\rho A_\text{eff})}{\sqrt{U^2+v_i^2+2Uv_i\sin(\beta-\gamma)}} \\ &= \frac{T/(2\rho A_\text{eff})}{\sqrt{(U\cos(\beta-\gamma))^2+(U\sin(\beta-\gamma)+v_i)^2}} \end{aligned}$$

Table 2: Cycloidal rotor flight regimes.

Regime	Subscript	Description
Hover	H	$U = 0$, so γ is irrelevant; $T > 0$, $v_i > 0$, with $\beta = 0$.
Forward Flight	F	$U > 0$, with $\gamma \approx 0$; $T > 0$, $v_i > 0$, with $0 < \beta < \pi/2$ because both lift and propulsive force need to be produced.
Forward Lift	L	$U > 0$, with $\gamma \approx 0$; $T > 0$, $v_i > 0$, with $\beta = 0$ because only lift needs to be produced.
Propulsion	P	$U > 0$, with $\gamma \approx 0$; $T > 0$, $v_i > 0$, with $\beta \approx \pi/2$ because thrust is now essentially aligned with forward flight speed.
Reverse Propulsion	RP	$U > 0$, with $\gamma \approx 0$; $T > 0$, $v_i > 0$, with $\beta \approx -\pi/2$ because thrust is now essentially aligned against forward flight speed.

We define the inflow coefficients,

(10)
$$\mu = \frac{U}{\Omega R}$$

(11)
$$\lambda = \frac{v_i}{\Omega R}$$

We also define a torque coefficient starting from the torque Q,

(12) $$C_Q = \frac{Q}{\rho(\Omega R)^2 RA},$$

and a power coefficient for $P = \Omega Q$

(13) $$C_P = \frac{P}{\rho(\Omega R)^3 A},$$

Still referring to Fig. 5, we define the rotation matrices that allow converting the vectors of reference frame to another.

To go from the rotating frame to the body frame, the rotation operator can be defined as

(14) $$\mathbf{R}_{\mathrm{br}} = \begin{bmatrix} \cos\theta & -\sin\theta \\ \sin\theta & \cos\theta \end{bmatrix}$$

In general we may expect θ to be small[2] so as a first approximation it is possible to say that

(15) $$\mathbf{R}_{\mathrm{br}} \approx \begin{bmatrix} 1 & -\theta \\ \theta & 1 \end{bmatrix}$$

The rotation matrix to transform a vector from the basic to the rotating frame is

(16) $$\mathbf{R}_{\mathrm{ro}} = \begin{bmatrix} \sin\psi & -\cos\psi \\ \cos\psi & \sin\psi \end{bmatrix}$$

2.2 Derivation

To start, it is necessary to compute the component of the air velocity with respect to the airfoil in the body reference frame. The flow velocity, $\mathbf{V}$, as seen from the body reference frame is thus,

(17)
$$\mathbf{V} = \mathbf{R}_{\mathrm{br}} \left(\begin{Bmatrix} \Omega R \\ 0 \end{Bmatrix} + \mathbf{R}_{\mathrm{ro}} \left(U \begin{Bmatrix} \cos\gamma \\ \sin\gamma \end{Bmatrix} + v_i \begin{Bmatrix} \sin\beta \\ -\cos\beta \end{Bmatrix} \right) \right)$$

As a consequence,

(18)
$$\begin{aligned} V_x = {} & \Omega R - \cos\psi(U\sin\gamma - v_i\cos\beta) \\ & + \sin\psi(U\cos\gamma + v_i\sin\beta) - \theta\Big(\cos\psi(U\cos\gamma \\ & + v_i\sin\beta) + \sin\psi(U\sin\gamma - v_i\cos\beta)\Big) \end{aligned}$$

(19)
$$\begin{aligned} V_y = {} & \theta\Big(\Omega R - \cos\psi(U\sin\gamma - v_i\cos\beta) \\ & + \sin\psi(U\cos\gamma + v_i\sin\beta)\Big) \\ & + \sin\psi(U\sin\gamma - v_i\cos\beta) + \cos\psi(U\cos\gamma + v_i\sin\beta) \end{aligned}$$

Assuming that $\Omega R \gg U$, $\Omega R \gg v_i$ and $|\theta| \ll 1$,

(20)
$$V_x \approx \Omega R$$

(21)
$$V_y \approx \theta\Omega R - v_i \sin(\psi - \beta) + U\cos(\psi - \gamma)$$

The angle of attack of the airfoil is

(22)
$$\alpha = \tan\frac{V_y}{V_x} \approx \frac{V_y}{V_x} \approx (\theta - \lambda\sin(\psi - \beta) + \mu\cos(\psi - \gamma))$$

Using the angle of attack it is possible to compute the lift and drag forces using a simple steady state and linear approximation,

(23)
$$D = \frac{1}{2}\rho V^2 c b C_{D_0}$$

(24)
$$L = \frac{1}{2}\rho V^2 c b C_{L/\alpha}\alpha$$

[2] This assumption is needed to simplify the formulas enough to make their analytical solution feasible; however, it might not hold in realistic operational cases, in which $|\theta|$ may grow to up to $\pi/4$ or so.

These two force components are in the wind reference frame (i.e. D parallel to the wind and L perpendicular), so they must be transformed in force components in the body reference frame,

(25)
$$F_{b_x} = -L\sin\alpha + D\cos\alpha \approx -L\alpha + D$$

(26)
$$F_{b_y} = L\cos\alpha + D\sin\alpha \approx L + D\alpha$$

Then, these two force components must be transformed in the rotating reference frame,

(27)
$$\begin{aligned} F_{r_x} &\approx F_{bx} + \theta F_{by} = -L\alpha + D + \theta L + \theta D\alpha \\ &\approx L(\theta - \alpha) + D \end{aligned}$$

(28)
$$\begin{aligned} F_{r_y} &\approx -\theta F_{bx} + F_{by} = \theta L\alpha - \theta D + L + D\alpha \\ &\approx L - D(\theta - \alpha) \end{aligned}$$

So, considering that $V^2 \approx (\Omega R)^2$,

(29)
$$\begin{aligned} \frac{F_{r_x}}{\rho(\Omega R)^2 cb/2} &= C_{L/\alpha}\left(\theta - \lambda\sin(\psi-\beta) + \mu\cos(\psi-\gamma)\right) \\ &\quad (\lambda\sin(\psi-\beta) - \mu\cos(\psi-\gamma)) + C_{D_0} \\ &= C_{L/\alpha}\left(\theta(\lambda\sin(\psi-\beta) - \mu\cos(\psi-\gamma)) \right. \\ &\quad \left. - (\lambda\sin(\psi-\beta) - \mu\cos(\psi-\gamma))^2\right) + C_{D_0} \end{aligned}$$

(30)
$$\begin{aligned} \frac{F_{r_y}}{\rho(\Omega R)^2 cb/2} &= C_{L/\alpha}\left(\theta - \lambda\sin(\psi-\beta) + \mu\cos(\psi-\gamma)\right) \\ &\quad - C_{D_0}(\lambda\sin(\psi-\beta) - \mu\cos(\psi-\gamma)) \end{aligned}$$

The imposed pitch angle is expressed as a harmonic series truncated at the second harmonic,

(31) $$\theta = \theta_0 + \sum_{n=1}^{2}\left(\theta_{cn}\cos n\psi + \theta_{sn}\sin n\psi\right)$$

The two force components can be expressed as truncated Fourier series as well,

(32)
$$F_{r_x} = F_{r_{x0}} + \sum_{n=1}^{N}\left(F_{r_{xcn}}\cos n\psi + F_{r_{xsn}}\sin n\psi\right)$$

(33)
$$F_{r_y} = F_{r_{y0}} + \sum_{n=1}^{N}\left(F_{r_{ycn}}\cos n\psi + F_{r_{ysn}}\sin n\psi\right)$$

Now, the constant part of the force tangential to the cylindrical path, $F_{r_{x0}}$, is computed by integration over a period. It will allow the calculation of the torque and thus the power required by the motor,

(34)
$$\begin{aligned} \frac{F_{r_{x0}}}{\rho(\Omega R)^2 cb/2} &= C_{D_0} - \frac{1}{2}C_{L/\alpha}\left(\mu^2 + 2\mu\lambda\sin(\beta-\gamma) + \lambda^2\right) \\ &\quad - \frac{1}{2}C_{L/\alpha}\left(\mu\cos\gamma + \lambda\sin\beta\right)\theta_{c1} \\ &\quad - \frac{1}{2}C_{L/\alpha}\left(\mu\sin\gamma - \lambda\cos\beta\right)\theta_{s1} \end{aligned}$$

and the torque coefficient is,

(35)
$$\frac{C_Q}{\sigma} = \frac{NF_{r_{x0}}R}{\rho(\Omega R)^2 AR}\frac{A}{Ncb} = \frac{1}{2}\frac{F_{r_{x0}}}{\rho(\Omega R)^2 cb/2}$$

or,

(36)
$$\begin{aligned} \frac{C_Q}{\sigma} &= \frac{1}{2}C_{D_0} - \frac{1}{4}C_{L/\alpha}\left(\mu^2 + 2\mu\lambda\sin(\beta-\gamma) + \lambda^2\right) \\ &\quad - \frac{1}{4}C_{L/\alpha}\left(\mu\cos\gamma + \lambda\sin\beta\right)\theta_{c1} \\ &\quad - \frac{1}{4}C_{L/\alpha}\left(\mu\sin\gamma - \lambda\cos\beta\right)\theta_{s1} \end{aligned}$$

The forces must be translated into the basic reference frame using the definition,

(37) $$\mathbf{T} = \mathbf{R}_{ro}^{T}\mathbf{F}_r$$

which gives,

(38)
$$T_x = \sin\psi F_{r_x} + \cos\psi F_{r_y}$$

(39)
$$T_y = -\cos\psi F_{r_x} + \sin\psi F_{r_y}$$

The total average force is given by the constant part of $\mathbf{T}$ times the number of blades N. Recalling the definition of the thrust coefficient, C_T, and of the solidity, σ, the following relations are obtained,

(40)
$$\begin{aligned} \frac{C_{T_x}}{\sigma} &= \frac{NT_{x0}}{\rho(\Omega R)^2 A}\frac{A}{Ncb} = \frac{T_{x0}}{\rho(\Omega R)^2 cb} \\ &= \frac{C_{L/\alpha}}{8}\Big(2\theta_{c1} \\ &\quad + \lambda(\cos\beta(2\theta_0 - \theta_{c2}) + \sin\beta(2 - \theta_{s2})) \\ &\quad + \mu(\cos\gamma(2 - \theta_{s2}) + \sin\gamma(-2\theta_0 + \theta_{c2}))\Big) \\ &\quad + \frac{C_{D_0}}{4}\left(\lambda\sin\beta + \mu\cos\gamma\right) \end{aligned}$$

(41)
$$\frac{C_{T_y}}{\sigma} = \frac{NT_{y0}}{\rho(\Omega R)^2 A}\frac{A}{Ncb} = \frac{T_{y0}}{\rho(\Omega R)^2 cb}$$
$$= \frac{C_{L/\alpha}}{8}\Big(2\theta_{s1} + \lambda(\cos\beta(-2-\theta_{s2}) + \sin\beta(2\theta_0+\theta_{c2})) + \mu(\cos\gamma(2\theta_0+\theta_{c2}) + \sin\gamma(2+\theta_{s2}))\Big) + \frac{C_{D0}}{4}(-\lambda\cos\beta + \mu\sin\gamma)$$

The force coefficient and direction are given by

(42)
$$C_T = \sqrt{C_{T_x}^2 + C_{T_y}^2}$$

(43)
$$\beta = -\arctan\frac{C_{T_x}}{C_{T_y}}$$

The force coefficient components, in wind axes, are

(44)
$$\frac{C_{T_\parallel}}{\sigma} = \frac{C_{T_x}}{\sigma}\cos\gamma + \frac{C_{T_y}}{\sigma}\sin\gamma$$

(45)
$$\frac{C_{T_\perp}}{\sigma} = -\frac{C_{T_x}}{\sigma}\sin\gamma + \frac{C_{T_y}}{\sigma}\cos\gamma$$

which yield

(46)
$$\frac{C_{T_\parallel}}{\sigma} = \frac{C_{L/\alpha}}{8}\Bigg(2\theta_{c1}\cos\gamma + 2\theta_{s1}\sin\gamma + \mu\Big(2+\sin(2\gamma)\theta_{c2} - \cos(2\gamma)\theta_{s2}\Big) + \lambda\Big(2\sin(\beta-\gamma) + 2\cos(\beta-\gamma)\theta_0 - \cos(\beta+\gamma)\theta_{c2} - \sin(\beta+\gamma)\theta_{s2}\Big)\Bigg) + \frac{C_{D0}}{4}(\lambda\sin(\beta-\gamma)+\mu)$$

(47)
$$\frac{C_{T_\perp}}{\sigma} = \frac{C_{L/\alpha}}{8}\Bigg(-2\theta_{c1}\sin\gamma + 2\theta_{s1}\cos\gamma + \mu\Big(2\theta_0 + \cos(2\gamma)\theta_{c2} + \sin(2\gamma)\theta_{s2}\Big) + \lambda\Big(-2\cos(\beta-\gamma) + 2\sin(\beta-\gamma)\theta_0 + \sin(\beta+\gamma)\theta_{c2} - \cos(\beta+\gamma)\theta_{s2}\Big)\Bigg) - \frac{C_{D0}}{4}\lambda\cos(\beta-\gamma)$$

This concludes the definition of the analytical aerodynamic cycloidal rotor model. The following section will present the implicit algebraic solution of these equations.

3. ALGEBRAIC SOLUTION

For the stated purpose of using the cycloidal rotor as a replacement part for the antitorque rotor of the helicopter, the two most important flight regimes that were considered are the Propulsion and Reverse Propulsion scenarios. These are the regimes in which the lateral cycloidal rotors work to provide the antitorque around the main rotor when there is no vertical component to the incoming wind. Furthermore, the cycloidal rotors used in this fashion can provide a net thrust. For both scenarios, the main interest is to know what power is required to obtain the wanted torque and thrust. The wanted thrust of each cycloidal rotor is found by the following procedure, where the original antitorque and forward thrust provided by the Bo-105 tail and main rotor are M_t and T_t, respectively.

First, the right, T_R and left, T_L, required thrusts are computed as,

(48) $$T_R = \frac{M_t + T_t d_L}{d_L + d_R}$$

and

(49) $$T_L = T_t - T_R$$

The power will be obtained by using Eq. (34) derived earlier as the input of,

(50) $$P = \left|\frac{F_{r_{x0}}}{\Omega RN}\right|$$

Equation (34) will be solved using the λ and C_T obtained from the procedure presented in the following two sections. The regime is Propulsion if the requested thrust is positive and Reverse Propulsion if the requested thrust is negative. Both regimes start from the definition of the Forward Flight mode of a cyclogyro. They differ from that regime because the perpendicular thrust, $C_{T_\perp}$, is set to null. This definition holds for cases where the main helicopter rotor takes all the antigravity forces.

3.1 Solving the Equations in Propulsion

In this configuration, the objective is to produce $C_{T_\perp} = 0$ and $C_{T_\parallel} = -C_{T_P} < 0$, i.e. $\beta = \pi/2$, with $\mu > 0$, $\gamma = 0$. Substituting these values into Eqs (46) and (47) yields

(51)
$$\begin{Bmatrix} -C_{T_P} \\ 0 \end{Bmatrix} = \frac{\sigma C_{L/\alpha}}{4}(\mu+\lambda_P)\begin{Bmatrix} 1 \\ \theta_0 \end{Bmatrix} + \frac{\sigma C_{L/\alpha}}{4}\begin{Bmatrix} \theta_{c1} \\ \theta_{s1} \end{Bmatrix} + \frac{\sigma C_{L/\alpha}}{8}(\mu+\lambda_P)\begin{bmatrix} 0 & -1 \\ 1 & 0 \end{bmatrix}\begin{Bmatrix} \theta_{c2} \\ \theta_{s2} \end{Bmatrix}$$

The collective pitch θ_0 is currently maintained at zero. Thus, a negative cosine one per revolution pitch, θ_{c1}, is used to produce the wanted negative horizontal force. This force pushes the rotor towards the left, opposite to the airstream direction. For now, a simple cycloidal rotor which uses only a single harmonic pitching motion is considered. Consequently, we set $\theta_{c2} = \theta_{s2} = 0$. Then, for a null perpendicular thrust and the conditions just stated,

(52)
$$\theta_{s1} = -(\mu+\lambda)\,\theta_0$$

which indicates that θ_{s1} is null. The inflow coefficient in this case is

(53)
$$\lambda_P = -\frac{\mu}{2} + \sqrt{\left(\frac{\mu}{2}\right)^2 + \frac{\pi C_{T_P}}{2}}$$

The solution of (51) with (53) is thus,

(54)
$$\left(\frac{\frac{-4C_{T_P}}{\sigma a} - \mu + \kappa\frac{\mu}{2} - \theta_c - \frac{C_d}{\sigma a}(\mu - \kappa\frac{\mu}{2})}{(\frac{C_d}{\sigma a}+1)\kappa}\right)^2 - \left(\left(\frac{\mu}{2}\right)^2 + \pi\frac{C_{T_P}}{2}\right) = 0$$

where a is $C_{L/\alpha}$ and κ is a term which integrates flow nonuniformity and tip losses in the equations. This term is inserted as a multiplier of the inflow terms when solving Eq (51). This method is inspired by the empirical factor of the Johnson[9] momentum theory in hover which uses $\lambda = \kappa\sqrt{C_T/2}$. The current κ is adapted to the cycloidal rotor by an approach similar to Yun *et al.*[5] which use an empirical multiplier on one term when solving their implicit inflow equation.

Now, the solution of Eq. (51) yields, when choosing the appropriate root,

(55)
$$\theta_{cP} = \frac{1}{(2a\sigma)}\left((a\kappa - 2a)\mu\sigma + (C_d\kappa - 2C_d)\mu - (a\kappa\sigma + C_d\kappa)\sqrt{2\pi C_{T_P} + \mu^2} - 8C_{T_P}\right)$$

if C_{T_P} is the known variable. Otherwise, if θ_c is the known variable we use,

(56)
$$\begin{aligned} C_{T_P} = {} & \frac{\pi a^2\kappa^2\sigma^2}{64} + \frac{\pi C_d^2\kappa^2}{64} + \frac{a\sigma\theta_{cP}}{4} + \frac{(C_d\kappa - 2C_d)\mu}{8} \\ & + \frac{\left(\pi C_d a\kappa^2 + 4(a\kappa - 2a)\mu\right)\sigma}{32} \\ & - \frac{(a\kappa\sigma + C_d\kappa)}{64}\left[\pi^2 a^2\kappa^2\sigma^2 + \pi^2 C_d^2\kappa^2 - 32\pi a\sigma\theta_c \right. \\ & + 16(\pi C_d\kappa - 2\pi C_d)\mu \\ & \left. + 64\mu^2 + 2\left(\pi^2 C_d a\kappa^2 + 8(\pi a\kappa - 2\pi a)\mu\right)\sigma\right]^{\frac{1}{2}} \end{aligned}$$

For further interest, the torque coefficient in this case is defined using,

(57)
$$\begin{aligned} \frac{C_Q}{\sigma} &= \frac{1}{2}C_{D_0} - \frac{1}{4}C_{L/\alpha}\left(\mu^2 + 2\mu\lambda + \lambda^2\right) \\ &\quad - \frac{1}{4}C_{L/\alpha}(\mu+\lambda)\,\theta_{c1} \\ &= \frac{1}{2}C_{D_0} + (\mu+\lambda)\frac{C_{T_P}}{\sigma} \end{aligned}$$

which yields,

(58)
$$C_Q = \frac{\sigma}{2}C_{D_0} + \left(\frac{\mu}{2} + \left(\left(\frac{\mu}{2}\right)^2 + \frac{\pi C_{T_P}}{2}\right)^{1/2}\right) C_{T_P}$$

Looking back at Eq. (34) one can see that, for this regime, θ_{s1} and θ_0 have no influence on the power consumed. This could be inspected in further details by resolving Eqs (46) and (47) with the intent of increasing thrust by changing the two aforementioned angles.

The solution for the Propulsion case works for all cases where the thrust pushes the rotor against the incoming wind and produces an inflow velocity v_i which has the same direction as the incoming velocity U. It will also work for cases where the inflow velocity is opposed to the incoming velocity up to a condition where the resulting velocity becomes null, such that $|U| = |v_i|$. There, it is expected that a vortex ring will occur. The Reverse Propulsion regime solution is used as soon as the required thrust changes direction. That solution is presented in the following section.

3.2 Solving the Equations in Reverse Propulsion

In the Reverse Propulsion case, everything is kept equal to the propulsion case, with the exception that $\beta = -\pi/2$. What thus happens is that the direction of the resulting mass flow rate is changed, and thus, to keep a positive value of that mass flow rate, the equations (7), (8), and (9) become, when setting $\gamma = 0$ and $\beta = -\pi/2$,

(59) $\dot{m} = (v_i - U)\rho A_{eff}$

which implies that,

(60) $T = (v_i - U)\rho A_{eff} 2v_i$

which when solved algebraically yields

(61) $v_i = \dfrac{-U \pm \sqrt{U^2 + \frac{4T}{2\rho A_{eff}}}}{2}$

respectively.

This latest equation has a real solution for any positive value of a thrust pointing to the right, which was not the case when the equation was solved for the Propulsion regime.

The positive root of Eq. (61) is kept because T and v_i need to have the same sign. That logic comes from the definitions of Fig. 5 and the fact that the rate of change of the momentum is equal to the thrust. Thus, the inflow parameter of the Reverse Propulsion case is,

(62)
$$\lambda_{RP} = -\frac{\mu}{2} + \sqrt{\left(\frac{\mu}{2}\right)^2 + \frac{\pi C_{T_{RP}}}{2}}$$

When setting for a null thrust perpendicular to the wind we obtain,

(63)
$$\begin{aligned}\left\{\begin{array}{c} -C_{T_{\mathrm{RP}}} \\ 0 \end{array}\right\} &= \frac{\sigma C_{L/\alpha}}{4}(\mu - \lambda_{\mathrm{RP}})\left\{\begin{array}{c} 1 \\ \theta_0 \end{array}\right\} \\ &+ \frac{\sigma C_{L/\alpha}}{4}\left\{\begin{array}{c} \theta_{c1} \\ \theta_{s1} \end{array}\right\} \\ &+ \frac{\sigma C_{L/\alpha}}{8}(\mu - \lambda_{\mathrm{RP}})\left[\begin{array}{cc} 0 & -1 \\ 1 & 0 \end{array}\right]\left\{\begin{array}{c} \theta_{c2} \\ \theta_{s2} \end{array}\right\}\end{aligned}$$

and thus,

(64)
$$\theta_{s1} = (\lambda_{\mathrm{RP}} - \mu)\,\theta_0$$

the equation to solve is thus,

(65)
$$\left(\frac{\frac{4C_{T_{RP}}}{\sigma a} - \mu - \kappa\frac{\mu}{2} - \theta_c - \frac{C_d}{\sigma a}(\mu + \kappa\frac{\mu}{2})}{(\frac{C_d}{\sigma a} + 1)\kappa}\right)^2 - \left(\left(\frac{\mu}{2}\right)^2 + \pi\frac{C_{T_{RP}}}{2}\right) = 0$$

where κ is the same empirical term defined in Section 3.2. Finally, solving Eq. (65) yields,

(66)
$$\begin{aligned} C_{T_{RP}} = &\frac{\pi a^2\kappa^2\sigma^2}{64} + \frac{\pi C_d^2\kappa^2}{64} + \frac{a\sigma\theta_{c_{RP}}}{4} + \frac{(C_d\kappa + 2C_d)\mu}{8} \\ &+ \frac{\left(\pi C_d a\kappa^2 + 4(a\kappa + 2a)\mu\right)\sigma}{32} \\ &- \frac{(a\kappa\sigma + C_d\kappa)}{64}\left[\pi^2 a^2\kappa^2\sigma^2 + \pi^2 C_d^2\kappa^2 + 32\pi a\sigma\theta_c\right. \\ &+ 16(\pi C_d\kappa + 2\pi C_d)\mu \\ &\left. + 64\mu^2 + 2\left(\pi^2 C_d a\kappa^2 + 8(\pi a\kappa + 2\pi a)\mu\right)\sigma\right]^{\frac{1}{2}}\end{aligned}$$

or, solving for θ_c when the pitch function is wanted and the required thrust is known,

(67)
$$\begin{aligned}\theta_{c_{RP}} = -\frac{1}{2a\sigma}\Bigg(&(a\kappa + 2a)\mu\sigma + (C_d\kappa + 2C_d)\mu \\ &- (a\kappa\sigma + C_d\kappa)\sqrt{2\pi C_{T_{RP}} + \mu^2} - 8C_{T_{RP}}\Bigg)\end{aligned}$$

where $C_{T_{RP}} = -C_{T_P} = C_{T_{||}}$.

4. CALIBRATION AND VALIDATION OF THE MODEL

Due to the absence of experimental data in forward flight, the Propulsion and Reverse Propulsion flight regime models are validated using hover experimental data. Three experimental dataset are available and are used to calibrate and validate the analytical propulsion models by imposing a null advance ratio. A dataset comes from Yun *et al.*[5] and another from IAT21,[10] which is a member of the CROP consortium. An experimental campaign was also run by Bosch Aerospace and reported by McNabb.[11] This last one had the particularity of using airfoils with a high drag coefficient which was reported by McNabb to be $C_{D_0} \approx 0.07$ and was used as such in the current algebraical model. Another difference between the three experimental setups is that the Bosch rotor transmitted movement to the blades by an apparatus located a midspan of the blades and covered by a cylindrical shell. The IAT21 experiments had a similar setup, but located at the external edges of the blades. The Yun *et al.* setup was positioned similarly to IAT21 but the arms were uncovered. Another noted difference is that the power measured by Yun *et al.* was the supplementary power required by the electrical drive when blades are added to the device. The power measured by McNabb is the power measured by a load cell. The power measured by IAT21 is the total motor power, for which they estimated a 5% total loss. The experimental data was thus taken as is from Yun *et al.* and McNabb and a 5% reduction was applied to the power measured by IAT21. Finally, IAT21 used NACA-0016 airfoils, as opposed to NACA-0012 for McNabb and Yun *et al.*. Even though the blades differed, a slope of the lift coefficient $a = C_{L/\alpha} = 6.04$ is used for all three configurations.

The other experimental parameters are briefly described in Table 3. Calibration was done by curve fitting the powers and thrusts obtained algebraically to the ones obtained experimentally. The results are shown in Figs 6 to 8.

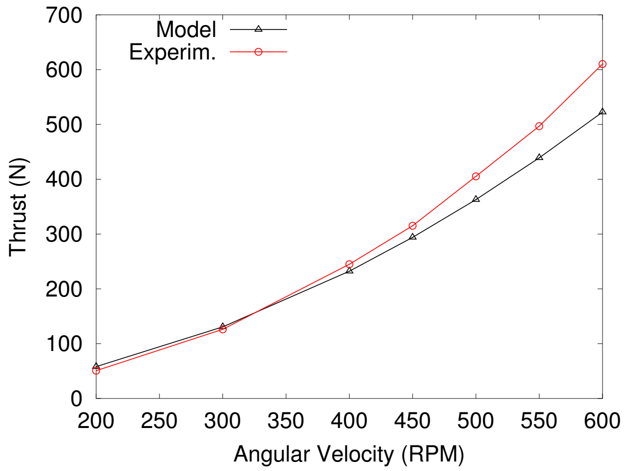

(a) Bosch T vs. Ω.

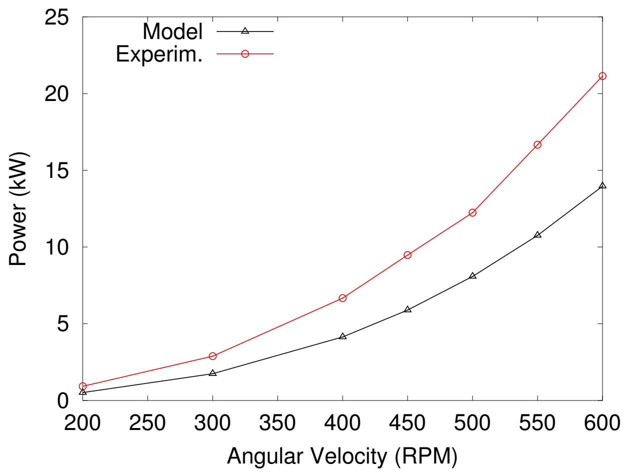

(b) Bosch P vs. Ω.

Figure 6: Comparison with the Bosch[11] experimental data of their 6 blade model at 25° magnitude pitch function. Using $\kappa = 1.0785$ and $C_{D_0} = 0.07$.

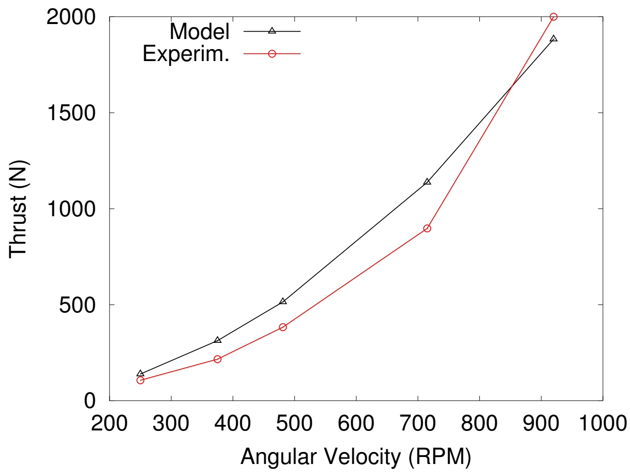

(a) IAT21 T vs. Ω.

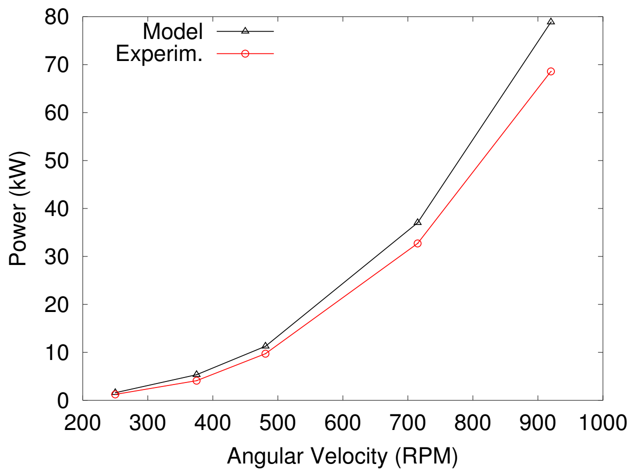

(b) IAT21 P vs. Ω.

Figure 7: Comparison with the IAT21 experimental data of the D-DALLUS L3 model at 37.5° magnitude pitch function. Using $\kappa = 1.2640$ and $C_{D_0} = 0.008$.

Although various weightings between power and thrust were tested, it was chosen to give an equal importance to both of them. Optimizing with a strong weight on power gave an excellent match for power, but yielded a very high κ, which is the only variable that is calibrated by the optimization. The smaller correctors κ required for the IAT21 and McNabb experimental data may be due to the fact that their experimental model had full cylinders which are known to reduce the tree-dimensionality of the flow. To verify this hypothesis, a previously developed three dimensional fluid dynamics model[8] is used to confirm the influence of the use of endplates on the rotor. A short description of the model along with the found effect of the endplates is presented in the following paragraph.

The OpenFOAM CFD toolkit has been relied upon to perform the fluid dynamic calculations. A laminar non-viscous solver is relied on since the main contributors to the thrust are the pressure induced forces. A double mesh interface which allows one to model a fixed angular velocity rotor zone and six embed periodically oscillating zones has been developed. A moving no-slip boundary condition was also developed to constrain the perpendicular velocity of the fluid at the foil to equal to the airfoil velocity and letting the parallel velocity uninfluenced. The timestep used for the simulations is variable and set to follow a Courant number of about 10. The mesh used without endplates has 366k cells while the one with endplates has 926k cells. The reason for such a big discrepancy is the difficulty of the snappyHexMesh meshing software to mesh surfaces close to interfaces and the thus related need to have a highly refined mesh in these zones. The spacing between the endplates and foils is one tenth of the chord length, which is

Table 3: Description of the experimental data.

Author	Radius R (m)	Span b (m)	Chord c (m)	Number of blades N	Threedimensional devices
Yun *et al.*[5]	0.4	0.8	0.15	6	Arms at edges
IAT21[10]	0.6	1.2	0.3	6	Cylinders at edges
Bosch[11]	0.610	1.22	0.301	6	Cylinder at midpoint

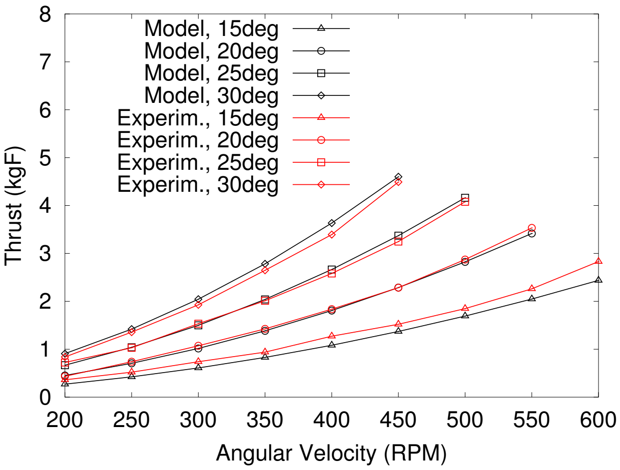

(a) Yun *et al.* T vs. Ω.

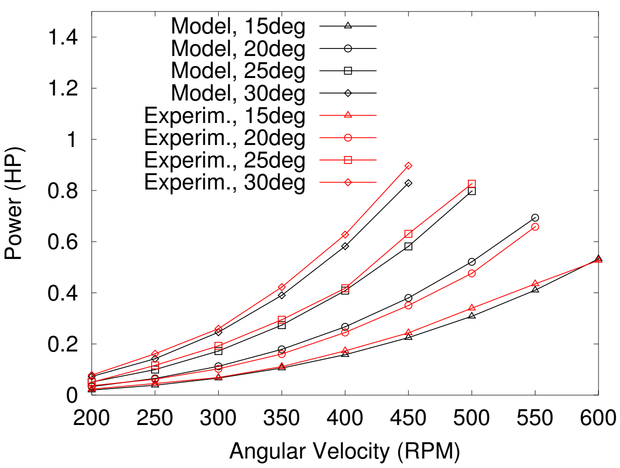

(b) Yun *et al.* P vs. Ω.

Figure 8: Comparison with the Yun *et al.*[5] experimental data of their baseline model at various pitching function magnitudes. Using $\kappa = 1.4804$ and $C_{D_0} = 0.008$.

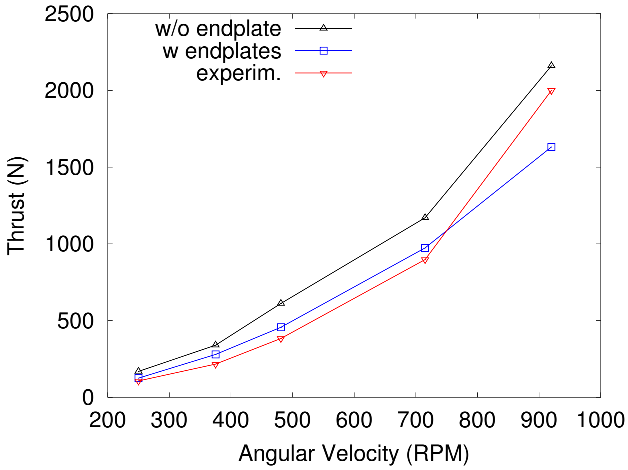

(a) IAT21 T vs. Ω.

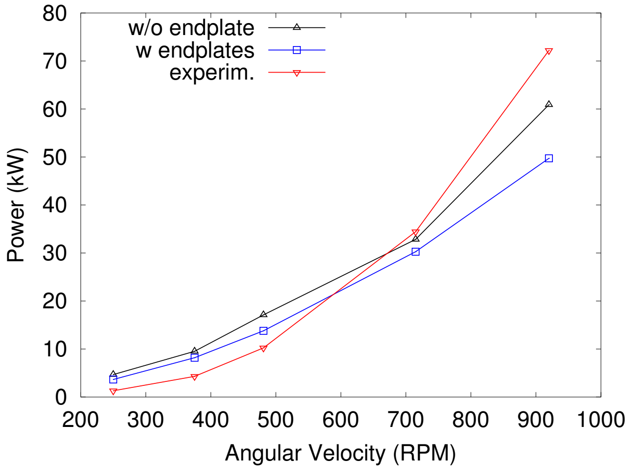

(b) IAT21 P vs. Ω.

Figure 9: Effect of the presence of endplates on the cycloidal rotor as confirmed by the 3D CFD simulations.

reported by Calderon *et al.*[12] to have the same effect as if it were attached to the foil.

The CFD results of the IAT21 L3 model at various angular velocities are shown with and without endplates on Fig. 9. They confirm the idea that the experimental apparatus used to transmit power will have an influence on the overall performance. In the experiment IAT21 used endplates. The instantaneous velocity fields and streamlines of the IAT21 L3 case where the pitch function angle magnitude is 37.5° at the angular velocity of 250 RPM are shown on Figs. 10(a) to 10(d). These figures further confirm the influence of the endplates geometry. Also, Fig. 10(d) confirms the fact reported by IAT21 that the flow enters the cycloidal rotor over an of 180 or more and exit over an arc of roughly 90°. Figure 10(c) agrees well with the findings of Yun *et al.*[5] that the flow is deviated by the rotor.

5. EFFICIENCY EVALUATION

As was stated in the introduction, of the three helicopter configurations proposed the most promising one is the helicopter with two lateral cycloidal rotors as shown in Figs 3(c) and 4. It has the advantage of reducing the demand on the

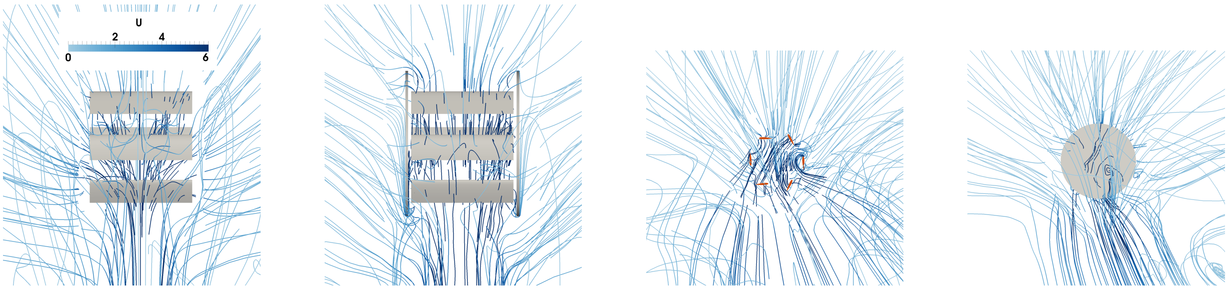

(a) Front view w/o endplates. (b) Front view with endplates. (c) Side view w/o endplates. (d) Side view with endplates.

Figure 10: Cycloidal rotor velocity streamlines from the CFD model at 250 RPM.

main rotor and this aspect will be studied in more depth in the current section. A first step consists of obtaining the performance characteristics of the Bo-105 helicopter.

5.1 Bo-105 Performance Characteristics

The performance characteristics of the original helicopter are shown in Figs 11 to 15. They consider diverse constant velocity advance ratios. They are obtained from a comprehensive aeroelastic helicopter model which takes into account the dynamics of the main rotor, the fuselage, and the tail rotor. That model is fully aeroelastic and provides torque and power figures for both main and tail rotors. It also yields the thrust they generate in magnitude and direction. A more complete description of the model can be found in a paper by Muscarello.[13] That same Bo-105 model was also used in a wind tunnel mode. There, the rotor was solidly fixed to the ground with a null pitch angle and was subjected to the same advance ratios and weight as the full helicopter. The data thus obtained gives the required power to provide anti-gravity alone and is used in the efficiency evaluation of the proposed design. Subtracting the power required by the main rotor to only provide lift at a null pitch angle from the power required by the full helicopter in trim yields the portion of power that is dedicated to forward propulsion. The resulting distribution of power shown on Fig. 12.

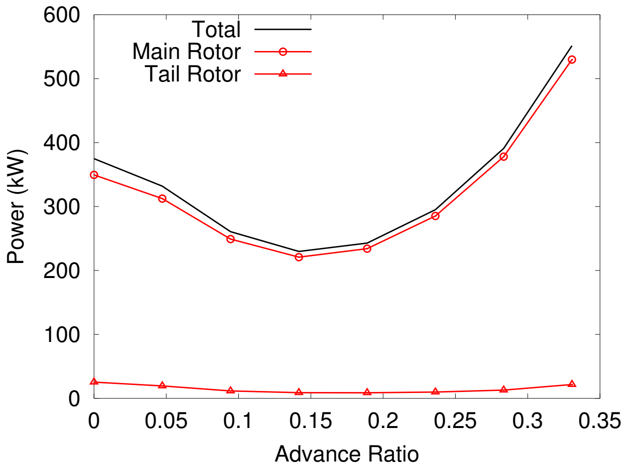

Figure 11: Power for the Bo-105 helicopter model.

5.2 First Optimization

The power demand of the full original Bo-105 helicopter is compared with that of the modified helicopter for identical advance ratios. This means the power demand of the main and tail rotor for the original helicopter and the power demand of the main and two lateral cycloidal rotors for the modified helicopter. To obtain a first pair of cycloidal rotors, an optimization of their performance characteristics was performed such as to obtain the required torque and thrust at the smallest expense of power.

Table 4 lists the parameters that were allowed to change during the optimization process. The maximum allowed angle of attack was set to 13.06°. Greater angles are no longer valid when using a constant slope lift coefficient. Furthermore, lift generation remains constant until 14.14° and then drops rapidly. This maximum angle of attack is obtained from Eq. (22) with $\gamma = 0$ and $\beta = \pi/2$. It becomes, after subbing in Eq. (31) truncated at the first harmonic term and Eq. (52),

(68)
$$\begin{aligned}\alpha &\simeq \theta_o + \theta_c \cos(\Psi) + \theta_s \sin(\Psi)\\ &\quad - \lambda \sin(\Psi - \pi/2) + \mu \cos\Psi\\ &\simeq \theta_o(1 - (\mu + \lambda)\sin\Psi) + (\theta_c + \lambda + \mu)\cos\Psi\end{aligned}$$

where the part which multiplies θ_o confirms the need for a null collective pitch. Indeed, the maximum and minimum values of the part of the equation multiplied by $\cos(\Psi)$ correspond to $\Psi = 0, \pi$. A non null θ_o at these values of Ψ can thus only increase that maximum angle of attack.

The maximum allowed distance between the centers of the two cycloidal rotors was 8.25 m and was chosen as such in order to prevent the cycloidal apparatus from extending further than the main rotor. The maximum distance is derived from,

$$\frac{d_L + D_R}{2} + b = \frac{d_L + D_R}{2} + d_L + D_R - L_W \leq D_{MR} \tag{69}$$

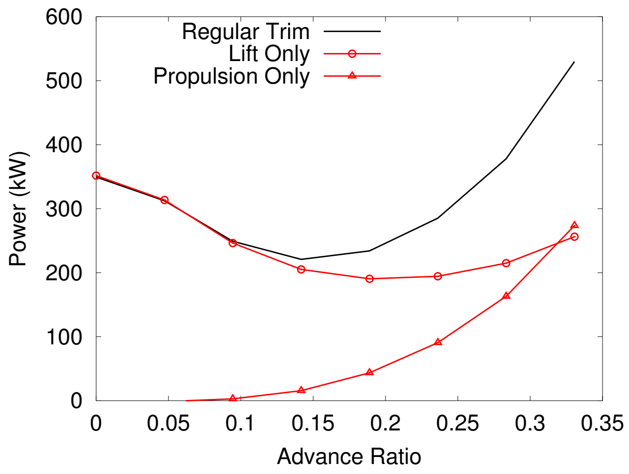

Figure 12: Power distribution of the main rotor.

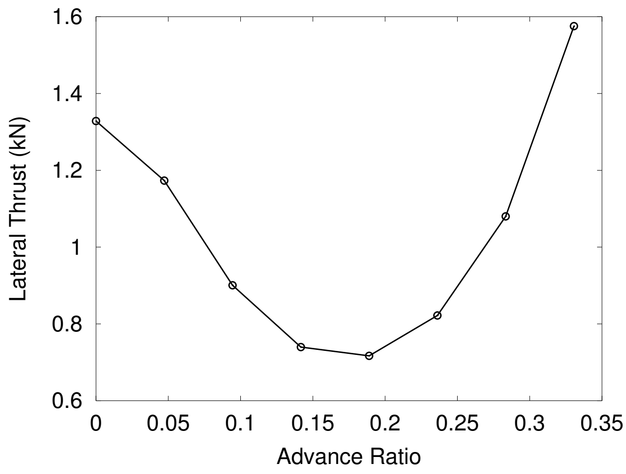

Figure 14: Lateral thrust produced from the Bo-105 helicopter model's tail rotor.

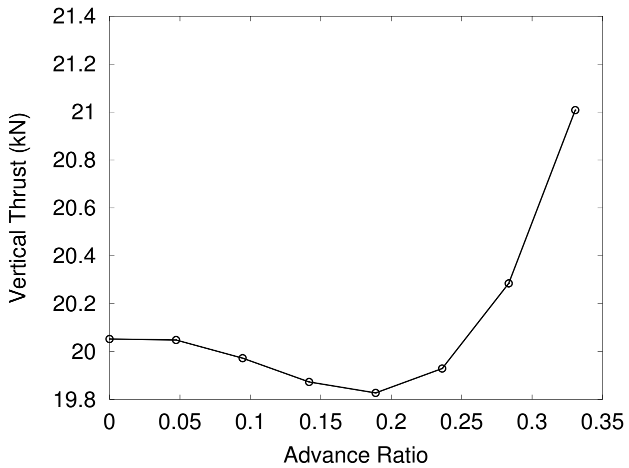

Figure 13: Vertical thrust produced from the Bo-105 helicopter model's main rotor.

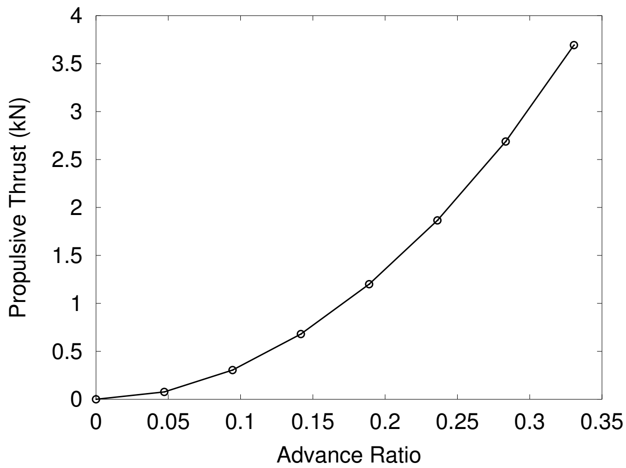

Figure 15: Propulsive thrust produced from the Bo-105 helicopter model.

where $D_{MR} = 9.84$ m and is the main rotor diameter and L_W is the width of the skids. Each rotor uses NACA-0012 airfoils and the rotor radii were limited to avoid any contact with the ground or the main rotor. The maximum tip velocity at maximum forward velocity was limited to Mach 0.85.

The first optimization lead to the data presented in Table 5 and gives the results show on Figs. 16 to 18. The angular velocity of the cycloidal rotors was not allowed to vary when changing advance ratio or flight regime, the pitch was restrained to a single harmonic variation, and the geometries of the two cycloidal rotors were identical.

These figures do consider the larger amount of power which is saved by the main rotor which does not have to pitch anymore. In fact, the main rotor only pitches in order to balance the position offset of its center of mass, but this might be set to be null if the center of mass and the rotors are aligned. Figures 17 and 18 show the provided thrust and anti-torque of cycloidal rotors and of the main or tail rotor, respectively. As required, the resulting torques and thrusts for both the original helicopter and the proposed design are equal.

5.3 Variable Angular Velocity

Taking the assumption that the cycloidal rotor could be powered electrically, it is reasonable to assume that the angular velocity of the rotors could be controlled independently and vary with advance ratio. Constraining the algorithm to use the same geometry found before and allowing each rotor to have a different angular velocity at each advance ratio considered yields a negligible increase in efficiency. The resulting power required for this configuration is shown in Fig. 19 and the optimal angular velocities of the rotors are shown in Fig. 20. Although the strange angular velocity distribution is shown, it was noticed that many angular velocity configurations yield similar results and that the limiting factor is the maximum allowed blade pitch an-

Table 4: Cycloidal rotors optimization properties.

	Radius R (m)	Midspan dist. $d_L + D_R$ (m)	Chord c (m)	N. of blades N	Ang. vel. Ω (RPM)
Lower Limit	0.1	0.5	0.05	3	20
Upper Limit	1.275	8.25	0.5	12	2000

Table 5: First optimization results.

Span b	f(dL)
Chord c	0.35368 m
Radius R	1.2452 m
Angular velocity Ω	397.15 RPM
Center to center distance d_{Lat}	9.4950 m
Number of blades N	3

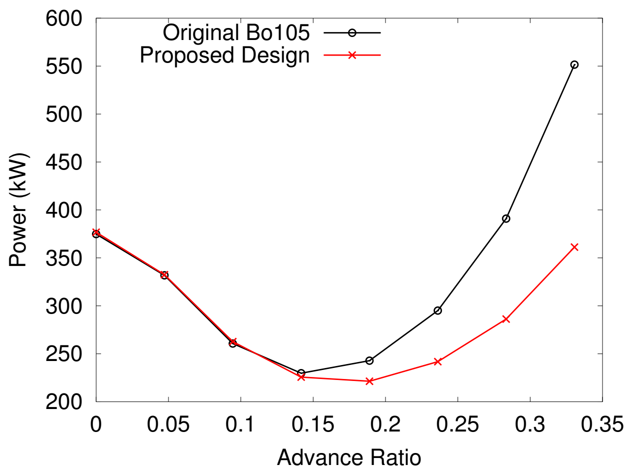

Figure 16: Total power of the original and new designs.

gle.

6. DISCUSSION

During the simulations it was noticed that, as expected, the optimizer will always tend to chose the largest pitch angles. This further confirms the advantage of using higher harmonic pitch controls to increase the portion of the cycle where the angle of attack is large. It was also noticed that changing the weighting used to minimize the power requirement of the cycloidal rotor does not have a significant influence on the results. Minimizing the power at high or low advance ratios does not have a noticeable influence of the resulting parameters and performance characteristics. As a security measure, the cycloidal rotor should be able to provide more thrust than shown in the figures in cases of emergency maneuvers. This is not expected to be a problem as slightly increasing the maximum angle of attack should reduce efficiency but increase thrust. If an electrical drive were used for the cycloidal rotors, it would be possible to have a variable angular velocity. Initial tests do however reveal that the efficiency increase of variable angular velocity rotors is negligible.

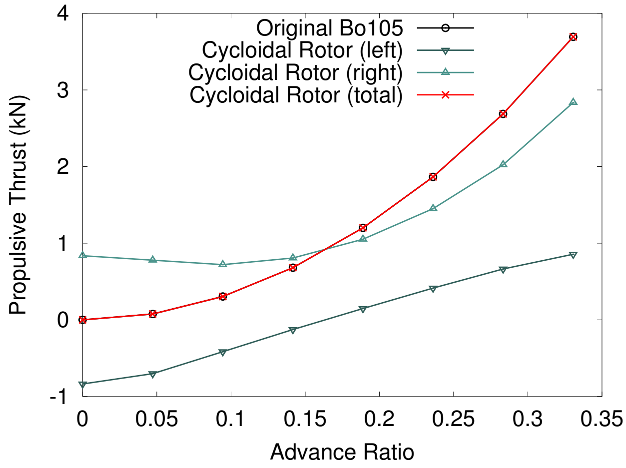

Figure 17: Propulsive thrust provided by the modified Bo-105 helicopter model.

A small influence of the resulting moment of the cycloidal rotors is expected. With the simple first design, a maximum combined cycloidal rotor moment of 850 Nm is expected. Quick calculations show that this could require at slight increase of main rotor power, reaching at most 10 kW. This is negligible when compared to the savings incurred. It is further reduced, or eliminated, by the reduced requirement for propulsion by the cycloidal rotors. Furthermore, a design where one of the cycloidal rotors rotates in the opposite direction would also reduce the induced moment. A more complete optimization, considering also main rotor trim, must be conducted to find the optimal configurations.

7. CONCLUSION

An algebraic model for the computation of the performance characteristics of a cycloidal rotor has been presented. It was validated against three sets of experimental data. It was used to assess the benefits of using cycloidal rotors as a replacement for the traditional tail rotor of a helicopter. Power savings of up to 50% are found. The dependence of efficiency on several design parameters have been highlighted. This provides useful indications for the design of the overall system. Analyses of increasingly detailed models of the cycloidal rotor concept are under way, focusing on propulsive efficiency, interference effects, and preliminary weight estimation. Future plans also include the use of the three dimensional CFD model to refine the current inflow model.

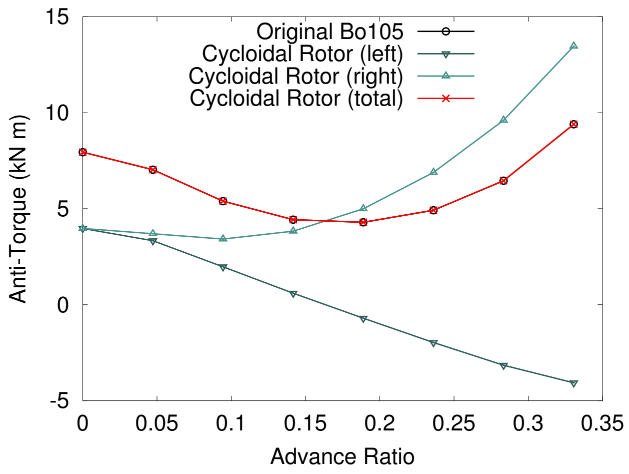

Figure 18: Anti-torque provided by the modified Bo-105 helicopter model.

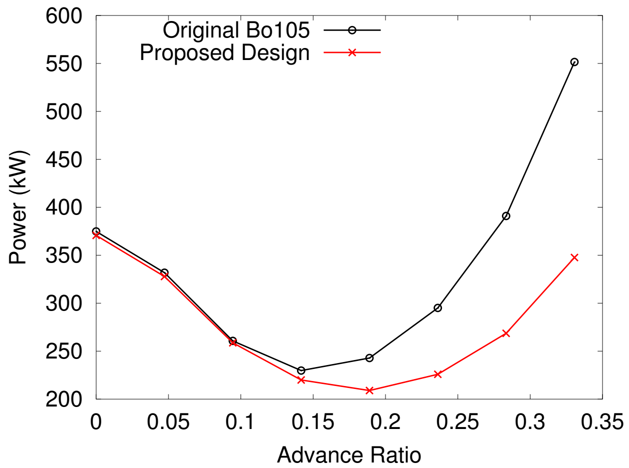

Figure 19: Total power of the original and variable angular velocity designs.

8. ACKNOWLEDGMENTS

The research leading to these results has received funding from the European Community's Seventh Framework Programme (FP7/2007–2013) under grant agreement N. 323047.

References

[1] I. S. Hwang, H. Y. Lee, and S. J. Kim. Optimization of cycloidal water turbine and the performance improvement by individual blade control. *Applied Energy*, 86(9):1532–1540, 2009.

[2] T. Maître, E. Amet, and C. Pellone. Modeling of the flow in a Darrieus water turbine: Wall grid refinement analysis and comparison with experiments. *Renewable Energy*, 51:497–512, 2013.

[3] M. El-Samanoudy, A. A. E. Ghorab, and S. Z. Youssef. Effect of some design parameters on the performance of a Giromill vertical axis wind turbine. *Ain Shams Engineering Journal*, 1(1):85–95, 2010.

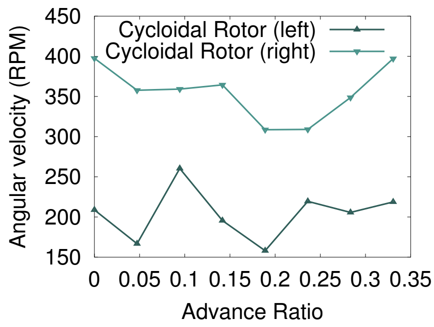

Figure 20: Angular velocity distribution for the variable design.

[4] Moble Benedict, Mattia Mattaboni, Inderjit Chopra, and Pierangelo Masarati. Aeroelastic Analysis of a Micro-Air-Vehicle-Scale Cycloidal Rotor. 49(11):2430–2443, 2011. doi:10.2514/1.J050756.

[5] C. Y. Yun, I. K. Park, H. Y. Lee, J. S. Jung, and I. S. H. Design of a New Unmanned Aerial Vehicle Cyclocopter. *Journal of the American Helicopter Society*, 52(1), 2007.

[6] G. Iosilevskii and Y. Levy. Experimental and Numerical Study of Cyclogiro Aerodynamics . *AIAAJ*, 44(12), 2006.

[7] L. Gagnon, M. Morandini, G. Quaranta, V. Muscarello, G. Bindolino, and P. Masarati. Cyclogyro Thrust Vectoring for Anti-Torque and Control of Helicopters. In *AHS 70th Annual Forum*, Montréal, Canada, May 20-22 2014.

[8] L. Gagnon, G. Quaranta, M. Morandini, P. Masarati, M. Lanz, C. M. Xisto, and J. C. Páscoa. Aerodynamic and Aeroelastic Analysis of a Cycloidal Rotor. In *AIAA Modeling and Simulation Conference*, June 16-20 2014.

[9] W. Johnson. *Helicopter Theory*. Dover Publications, New York, 1994.

[10] C. M. Xisto, J. C. Páscoa, J. A. Leger, P. Masarati, G. Quaranta, M. Morandini, L. Gagnon, D. Wills, and M. Schwaiger. Numerical modelling of geometrical effects in the performance of a cycloidal rotor. In *6th European Conference on Computational Fluid Dynamics*.

[11] M. L. McNabb. Development of a Cycloidal Propulsion Computer Model and Comparison with Experiment. Master's thesis, 2001.

[12] D. E. Calderon, D. Cleaver, Z. Wang, and I. Gursul. Wake Structure of Plunging Finite Wings. In *43rd AIAA Fluid Dynamics Conference*, June 24-27 2013.

[13] V. Muscarello, P. Masarati, G. Quaranta, L. Lu, M. Jump, and M. Jones. Investigation of Adverse Aeroelastic Rotorcraft-Pilot Coupling Using Real-Time Simulation. In *AHS 69th Annual Forum*, Phoenix, Arizona, May 21–23 2013. Paper No. 193.